



# Nanoscale

## Probing ballistic thermal conduction in segmented silicon nanowires

Journal:	<i>Nanoscale</i>
Manuscript ID	NR-ART-05-2019-003863.R2
Article Type:	Paper
Date Submitted by the Author:	28-Jun-2019
Complete List of Authors:	Anufriev, Roman; The University of Tokyo, IIS Gluchko, Sergei; The University of Tokyo, IIS Volz, Sebastian; COMUE Universite Paris-Saclay; University of Tokyo Nomura, M.; Univ Tokyo

SCHOLARONE™  
Manuscripts

# Probing ballistic thermal conduction in segmented silicon nanowires

Roman Anufriev<sup>1,\*</sup>, Sergei Gluchko<sup>1,2</sup>, Sebastian Volz<sup>1,2</sup>, & Masahiro Nomura<sup>1,3,\*</sup>

<sup>1</sup> Institute of Industrial Science, The University of Tokyo, Tokyo 153–8505, Japan.

<sup>2</sup> Laboratory for Integrated Micro Mechatronic Systems / National Center for Scientific Research-Institute of Industrial Science (LIMMS/CNRS-IIS), The University of Tokyo, Tokyo 153–8505, Japan.

<sup>3</sup> CREST, Japan Science and Technology Agency, Saitama 332–0012, Japan.

\*Correspondence should be addressed to R.A. (email: anufriev@iis.u-tokyo.ac.jp) or M.N. (email: nomura@iis.u-tokyo.ac.jp).

## Abstract

Ballistic heat conduction in semiconductors is a remarkable but controversial nanoscale phenomenon, which implies that nanostructures can conduct thermal energy without dissipation. Here, we experimentally probed ballistic thermal transport at distances of 400 – 800 nm and temperatures of 4 – 250 K. Measuring thermal properties of straight and serpentine silicon nanowires, we found that at 4 K heat conduction is quasi-ballistic with stronger ballisticity at shorter length scales. As we increased the temperature, quasi-ballistic heat conduction weakened and gradually turned into diffusive regime at temperatures above 150 K. Our Monte Carlo simulations illustrate how this transition is driven by different scattering processes and linked to the surface roughness and the temperature. These results demonstrate the length and temperature limits of quasi-ballistic heat conduction in silicon nanostructures, knowledge of which is essential for thermal management in microelectronics.

## Introduction

Ballistic phonon transport is a remarkable nanoscale phenomenon with potential applications in thermal management<sup>1,2</sup> and optomechanics<sup>3,4</sup> at room temperature, as well as in low-temperature sensors<sup>5,6</sup> and systems for quantum informatics<sup>7–9</sup>. In crystals, some phonons can preserve their phase as they travel over hundreds of nanometers<sup>10,11</sup> and reflect from crystal boundaries<sup>12,13</sup>. Due to such a long lifetime and the elastic reflections, phonons can transport energy over long distances without dissipation. In semiconductors, where phonons play the role of heat carriers, such phonon transport results in non-diffusive conduction of heat<sup>14</sup>. In nanostructures, phonons can even cross without resistance the entire structure or at least cover its significant part, thus participating in ballistic or at least quasi-ballistic heat conduction<sup>15</sup> and violating Fourier's law<sup>16</sup>.

Signs of such unusual heat conduction appear in experiments on various nanostructures, such as Si<sup>15,17–19</sup>, SiGe<sup>20–22</sup>, and Ta<sub>3</sub>Pd<sub>3</sub>Se<sub>8</sub><sup>23</sup> nanowires (NWs), carbon nanotubes<sup>24–26</sup>, and graphene ribbons<sup>27,28</sup>. However, the experiments usually involve non-negligible thermal contact resistance<sup>21,22,29</sup>, and some studies were criticised for mistakenly attributing their observations to ballistic heat conduction<sup>21,29,30</sup>. For example, some authors suggested<sup>18,21</sup> that the previous observations of non-linear resistance in silicon membranes<sup>31</sup> and NWs<sup>18</sup> at room temperature might be caused by the thermal contact resistance or other resistive processes. Indeed, several recent experiments<sup>17,22,32,33</sup> showed purely diffusive heat conduction in silicon NWs at room temperature, with ballistic contribution visible only at lower temperatures<sup>15,17</sup>. Thus, ballistic thermal conduction in silicon remains a controversial topic due to the metrological issue of contact resistance.

To avoid this and other metrological issues, one can use contactless optical experiments and comparative study design. Previously, Heron *et al.*<sup>34</sup> proposed to compare straight and serpentine NWs to observe phonon blocking effect, which implies ballistic phonon transport, at ultra-low temperatures. In this work, we probe ballistic heat conduction in silicon NWs in a broad

temperature range using a comparative design, inspired by Heron *et al.*<sup>34</sup>, and contactless method that avoids parasitic thermal contact resistance. This allows us to reliably observe signs of ballistic thermal transport by directly comparing the time of heat dissipation through straight and serpentine NWs. Studying different NW dimensions and temperatures, we discuss the length scales and temperatures at which heat conduction remains quasi-ballistic in silicon nanostructures.

## Experimental

To prepare our samples, we used conventional top-down fabrication methods applied to a silicon-on-insulator wafer with 145-nm-thick top silicon monocrystalline layer (Methods). Each sample consisted of four NWs supporting a suspended island with Al pad, which acts as both heater and detector (Fig. 1a). We designed this study as comparative and prepared pairs of samples with serpentine (Fig. 1b) and straight (Fig. 1c) NWs. The serpentine NWs consisted of seven equal segments, each of the length  $L_S$ , and had the same total length as their straight pair. To study ballistic heat conduction at different length scales, we prepared pairs of samples with different segment lengths ( $L_S$ ) and thus different corresponding total lengths ( $L$ ).

To measure the thermal properties of our NWs, we used the micro time-domain thermoreflectance technique ( $\mu$ TDTR). In our setup, a pulsed “pump” laser periodically heats the Al pad placed on the suspended island in the centre of each sample. The heat brought by each pulse dissipates from the island through the NWs towards the surrounding wafer, which acts as a heat sink. Since the reflectance of the Al pad changes proportionally to its temperature, we can monitor heat dissipation from the island by continuously measuring the intensity of the second “probe” laser reflected from the Al pad (Methods). Figure 1d shows examples of decay curves measured for straight and serpentine NWs measured at 4 K. To quantitatively compare the decay curves, we fit them with an exponential function  $\exp(-t/\tau)$ , from which we can extract the decay time ( $\tau$ ).

To extract the thermal conductivity from the measured decay time, we performed the finite element method (FEM) simulations of this experiment. In the simulations, we used the value of thermal conductivity as a parameter to fit the experimentally measured decay curve by the curve from the

simulation, thus finding the thermal conductivity corresponding to the experimental data. For each sample, we fabricated and measured two additional copies. Hence, data points in this work show the average of three measurements, with the error bars indicating the standard deviation (Methods). More details on the sample fabrication and the experimental method can be found in our previous works<sup>35–37</sup>.

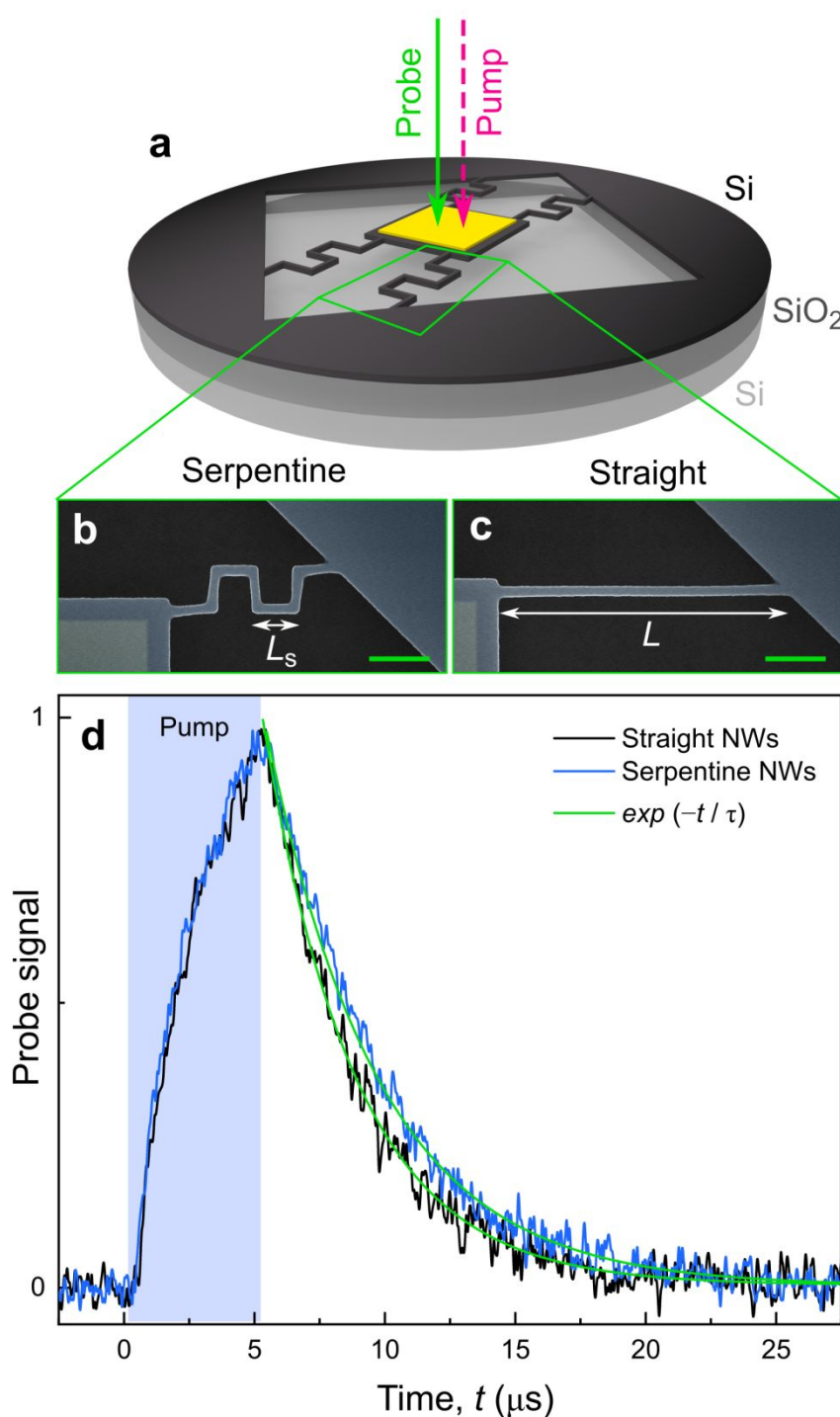


**Fig. 1** (a) Schematics of a sample. SEM images of samples with (b) serpentine and (c) straight NWs. Scale bars are 1  $\mu\text{m}$ . (d) The decay curves for straight and serpentine NWs measured at 4 K

and fitted with exponential functions. The fitting curves show that decay time for serpentine NW is longer.

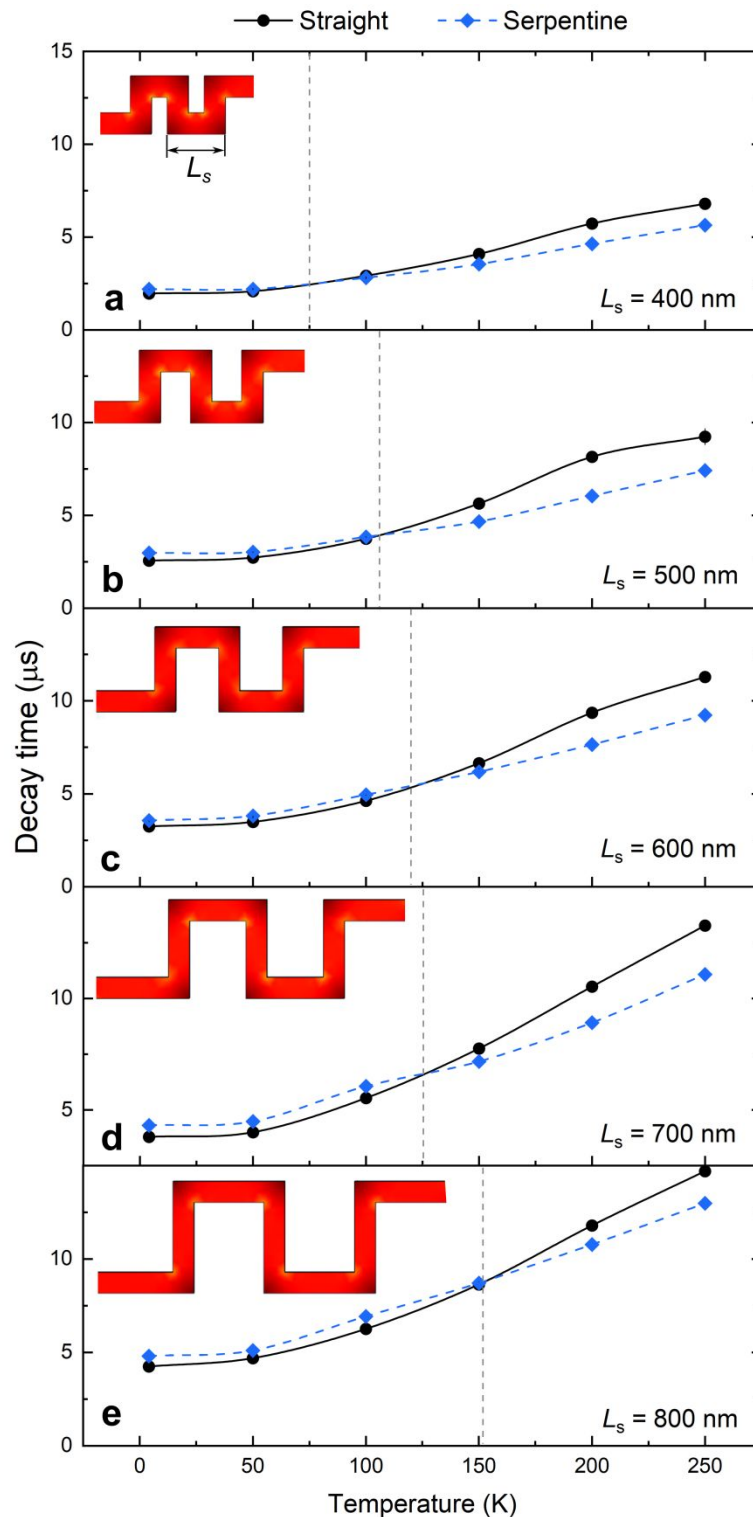
### Ballistic conduction in different geometries

Figure 2 shows the decay times for all samples measured at temperatures in the 4 – 250 K range. At 4 K, decay times in aligned NWs are shorter than in serpentine. In other words, heat dissipation is slower in serpentine NWs. We explain this difference by the presence of ballistic phonon transport, which is limited in the serpentine NWs due to the phonon scattering on the sidewalls at the turns.

As we increase the temperature, the ballistic effects weaken and the decay times inverse, so that heat dissipation in straight NWs becomes slower. This inversion occurs because in the diffusive regime heat flows to the heat sink through the most direct path. This path is shorter in serpentine than in straight NWs because heat flux cuts corners in serpentine geometry<sup>15</sup>□, as illustrated by the finite element method simulations in the insets of the Fig. 2. The simulations show that heat fluxes follow a zigzag pattern inside the serpentine NWs, as if cutting the corners, and thus reach the heat sink faster. The strength of this corner-cutting effect depends on the segment length ( $L_S$ ). Naturally, the effect is stronger in shorter segments, and the inversion of decay times occurs at lower temperatures. As we increase the segment length, the effect weakens, the zigzag pattern becomes less clear, and the inversion takes place at higher temperatures, as shown by dashed vertical lines in Fig. 2.

To eliminate the corner-cutting effect, we extracted the thermal conductivity using FEM modelling, which takes the shape of heat flux path into account. Figure 3 gives an example of the extracted thermal conductivity for the measurements at 4 K. All the straight NWs show the thermal conductivity of about  $0.018 \text{ Wm}^{-1}\text{K}^{-1}$ . Such a low thermal conductivity in NWs as compared to bulk silicon ( $> 100 \text{ Wm}^{-1}\text{K}^{-1}$ ) is determined by the low heat capacity and strong impact of the surface phonon scattering at 4 K. This value is 10% lower than measured in our previous work<sup>15</sup>□

due to the visibly higher surface roughness. The serpentine NWs show lower thermal conductivity than the straight NWs. Moreover, the thermal conductivity depends on the segment length ( $L_s$ ).



**Fig. 2** Thermal decay time in straight and serpentine NWs inverses as the temperature grows, and the effect depends on the segment lengths ( $L_s$ ). The intersection point (dashed vertical lines) drifts with temperature. The insets show the finite element method simulations of the heat fluxes in the serpentine NWs, illustrating the corner-cutting effect.

On the one hand, we can discuss this length dependence using phonon mean free path: Since lengths of free phonon flights are limited by the length of one segment<sup>15</sup>, the thermal conductivity naturally depends on the segment length. On the other hand, we can consider the length dependence as a sign of ballistic heat conduction within each segment. Indeed, experiments on serpentine NWs essentially probe the thermal conductivity of individual segments connected in sequence *via* diffusive junctions. Thus, the thermal conductivity of serpentine NWs behaves like that of short straight NWs.

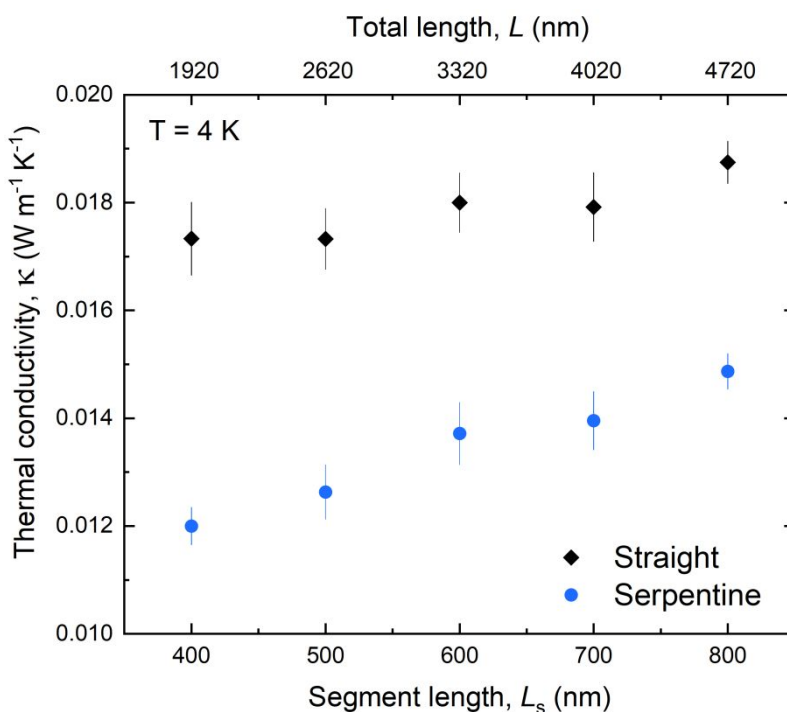


**Fig. 3** Thermal conductivity of serpentine NWs is lower than that of straight NWs and depends on segment length.

To illustrate this point of view, we plot the thermal conductivity of the segments together with our data on straight NWs measured in our previous work<sup>15</sup> for a wide range of lengths (Fig. 4). The data measured on serpentine NWs seem to complement the data measured on straight NWs<sup>15</sup>, and the thermal conductivity of the serpentine NWs with segment length  $L_s = 800$  nm is almost identical to that of straight NW with the total length  $L = 775$  nm. The thermal conductivity

data form a length-dependent trend, which indicates the presence of ballistic heat conduction.

Measurements at higher temperatures revealed similar trends (Fig. S1).

To verify that this trend is not caused by some parasitic resistance<sup>21,29</sup>, we also plot the thermal resistance per unit area (Fig. 4), given by  $A / K$ , where  $A$  is a cross-section area and  $K$  is the thermal conductance. The data points measured on serpentine NWs deviate from the linear trend ( $A / K \sim L$ ) while longer ( $> 2 \mu\text{m}$ ) NWs follow the linear trend that indicates diffusive heat conduction. Thus, we can consider the measurements on the serpentine NWs as a method to probe heat conduction in short NWs.

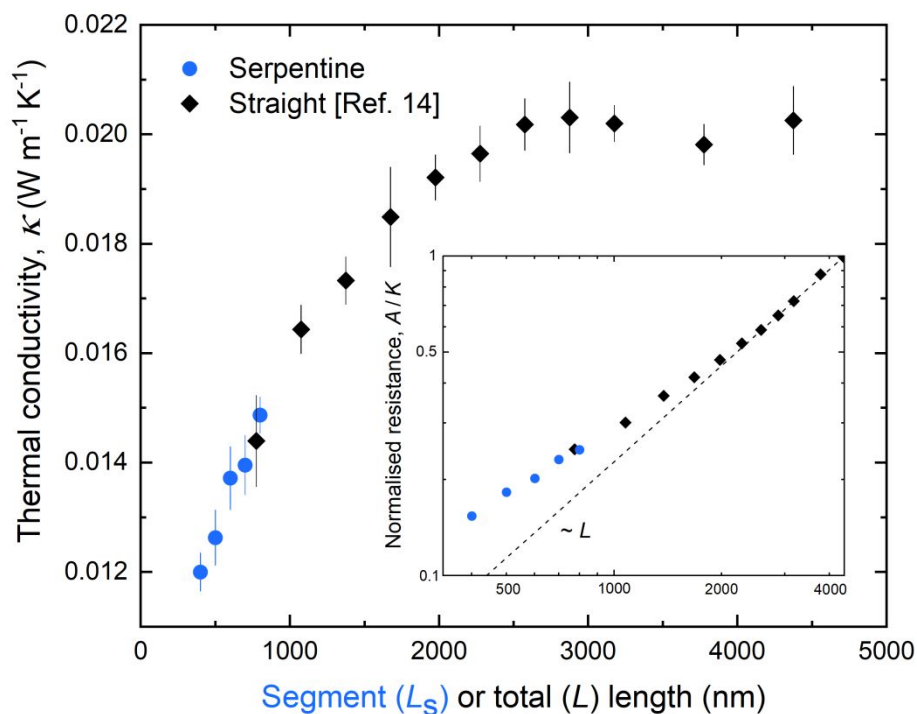


**Fig. 4** Length-dependent thermal properties. The thermal conductivity of serpentine NWs and straight NWs from Ref.<sup>15</sup> measured at 4 K form a common length-dependent trend, which indicates quasi-ballistic heat conduction. The inset shows that the normalised thermal resistance per unit area deviates from a linear trend.

### Length and temperature scales of ballistic conduction

Regardless of our point of view on the segment-length dependence, the difference in thermal conductivity of straight ( $\kappa_{\text{straight}}$ ) and serpentine ( $\kappa_{\text{serpentine}}$ ) NWs indicates quasi-ballistic heat conduction regime. Thus, analyzing the  $\kappa_{\text{straight}} / \kappa_{\text{serpentine}}$  ratio, we can characterise the strength of ballistic heat conduction at the length scale comparable with the segment length ( $L_S$ ). Figure 5

shows the  $\kappa_{\text{straight}} / \kappa_{\text{serpentine}}$  ratio for different segment lengths and temperatures. At 4 K, as segments become shorter, the ratio increases and reaches 1.4 for the shortest segments of 400 nm in length. Similar dependence on the segment length has been predicted theoretically<sup>38</sup>. However, as we increase the temperature, this trend flattens, and the ratio gradually reduces to one at 150 K and higher. These measurements show that temperature has a substantial impact on the presence of ballistic heat conduction.

To study this effect in more details, we replot the data as a function of temperature.

Figure 5b shows that the  $\kappa_{\text{straight}} / \kappa_{\text{serpentine}}$  ratio decreases for all segment lengths alike and reaches one at about 150 K. In our previous work<sup>15</sup>, a similar transition occurred but at the temperature of 200 K due to lower surface roughness.

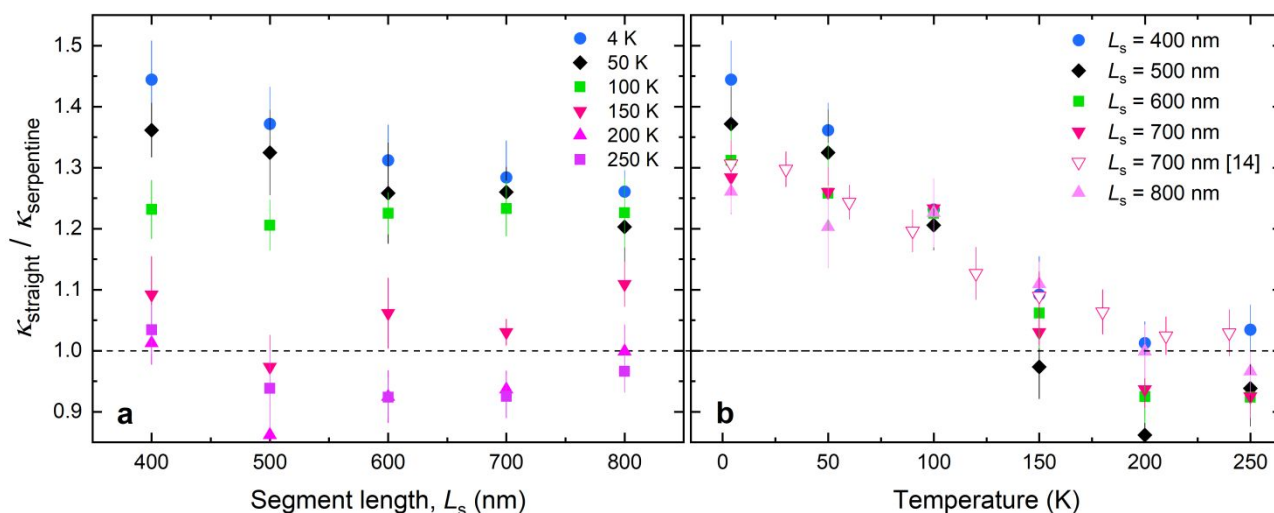


**Fig. 5** Transition from quasi-ballistic to diffusive heat conduction. The relative thermal conductivity of pairs of NWs (a) with different segment lengths measured and (b) at different temperatures show that signs of ballistic heat conduction disappear above 150 K.

### Phonon transport simulations

To better understand heat conduction in our NWs, we conducted Monte Carlo simulations (Methods) of phonon transport in a three-dimensional model of serpentine NWs (Figs. 6a-c). First, we study where and how phonons are scattered at different temperatures. Figures 6d-f show points of diffuse surface scattering (blue), specular surface scattering (green), and internal phonon-phonon scattering (red) events at different temperatures.

At 4 K, scattering events are mainly specular. At the polished top and bottom surfaces of the wafer only 1.5% of scattering events are diffusive, so these surfaces have a negligible impact on heat conduction. At the rougher side walls, the scattering is more diffusive (37 %). The histograms in Figs. 6d-f show the relative number of diffuse and specular scattering events at the upper sidewall. The histogram at 4 K highlights that the phonon back-scattering on the upper sidewall is especially prominent near the corner, where the sidewall is perpendicular to incoming heat flux. At 50 K, specular scattering weakens, and sidewall scattering becomes 98% diffusive. Moreover, rare phonon-phonon scattering events occur. At 100 K, surface scattering becomes 99% diffusive whereas phonon-phonon scattering now constitutes 41% of all scattering events. Table S1 lists the exact percentages of each scattering type and Fig. S2 shows scattering maps for the surface roughness of 1 nm. These scattering maps illustrate a temperature-driven transition from the quasi-ballistic regime with mainly specular surface reflections to the diffusive regime with internal and diffuse surface scattering dominating phonon transport. This transition explains why the impact of the corners disappears at higher temperatures.

Let us now study the impact of corners more quantitatively. Figure 6g shows how far phonons can travel along the axis of serpentine NWs between diffuse scattering events at 4 K. The peaks at 400, 600, and 800 nm correspond to segment lengths and show that many phonons are freely flying inside one segment but are back-scattered from the perpendicular wall at segment end. Nevertheless, most phonons seem to be scattered before they reach the end of a segment. Indeed, the distributions reach maxima at zero, showing that many phonons do not travel along the NW axis at all. To clarify this feature, we also plot original lengths of phonon flights, not projected on the NW axis (Fig. 6h). Whereas the peaks corresponding to the segment lengths are still visible, a common dominant peak appears at 155 nm — the width of our NWs. This peak shows that most of the scattering events occur on the NW side walls. In other words, the phonons transport is mainly controlled by the scattering on NW sidewalls, whereas turns of the serpentine NWs play a

secondary role even at 4 K. The situation is qualitatively the same even for lower surface roughness (Fig. S3).

However, the surface quality plays a critical role in the scattering on sidewalls at 4 K. Figure 6i shows that as we reduce surface roughness ( $\eta$ ), phonon flights become longer. For a realistic value  $\eta = 0.5$  nm the length distribution becomes almost flat. Thus, improving surface quality makes ballisticity stronger. Despite that importance of surface roughness, the most substantial impact on the phonon flight lengths comes from temperature. Figure 6j shows that the distribution drops by orders of magnitude as we increase the temperature from 4 to 100 K. As we saw earlier, the impact of temperature is related to both more diffusive surface scattering and more frequent internal scattering events. The plot also shows that even improving surface roughness cannot compensate for these temperature-induced changes. The curves for surface roughness of 1 and 2 nm are noticeably different only at 4 K but not at higher temperatures.

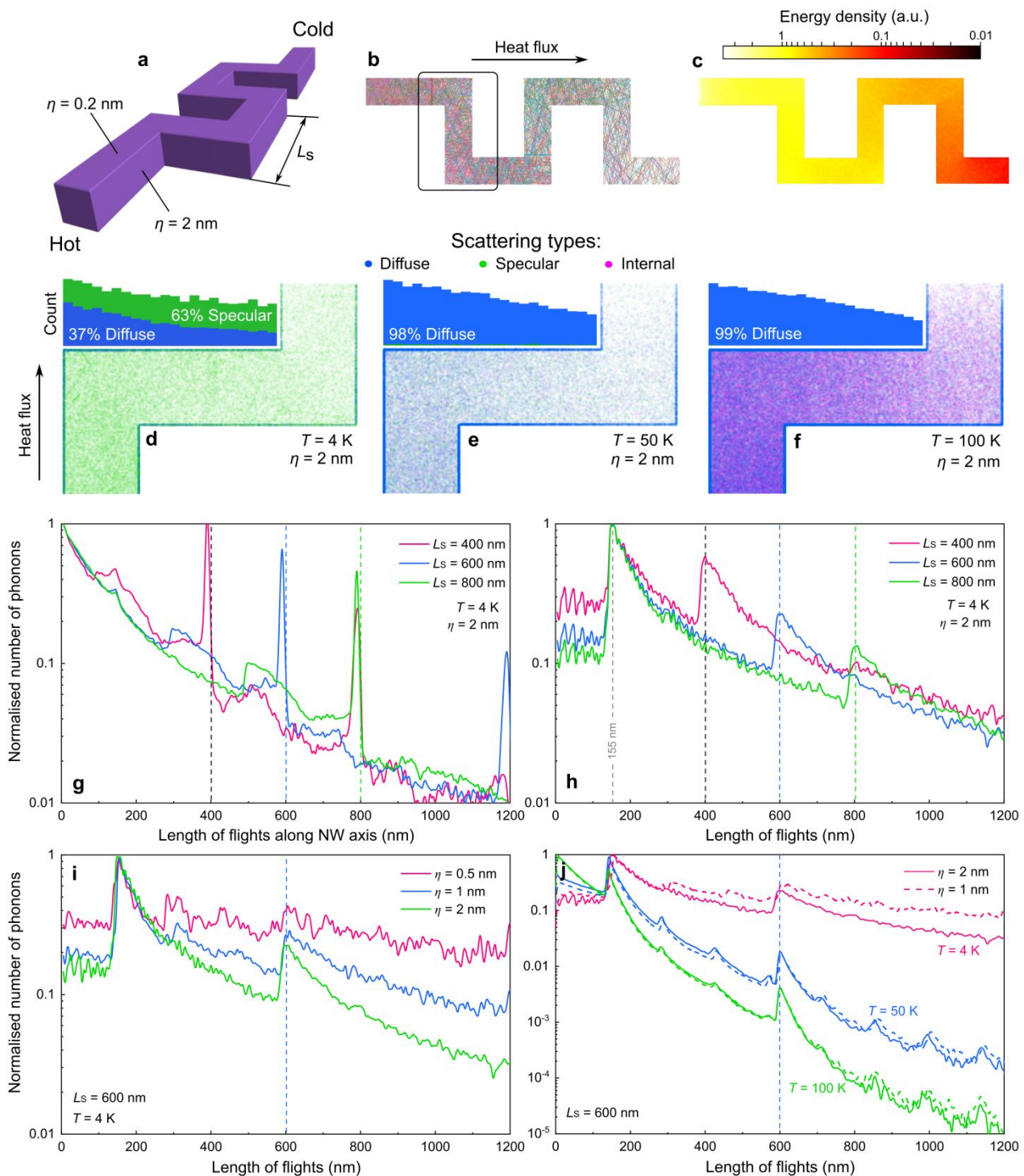


**Fig. 6** (a) Schematic of the simulation model. Example of (b) phonon trajectories and (c) thermal energy density map at 4 K in the steady state regime. Maps of diffuse (blue), specular (green), and internal (red) scattering events at (d) 4 K, (e) 50, and (f) 100 K. (g) The normalised number of phonons as a function of phonon flight lengths projected on NW axis. The original length of phonon flights for different segment lengths (h), the surface roughness (i), temperatures (j).

## Discussion and conclusions

In this work, we compare heat conduction in straight and serpentine NWs under various conditions. Like in the pioneering experiments by Heron *et al.*<sup>34</sup>, we find that turns of serpentine

NWs partly block thermal transport at low temperatures. At 4 K, serpentine NWs are less thermally conductive than straight NWs of the same length, and the difference depends on the length of segments in serpentine NWs. We attribute faster heat dissipation in straight NWs to the presence of ballistic phonon transport, which is interrupted by the back-scattering at the turns of serpentine NWs.

Indeed, the average phonon wavelength at 4 K is about 25 nm<sup>17</sup>, whereas phonon mean free path in bulk silicon is much longer than the segment-length<sup>11,39</sup>. As such, phonons may travel experiencing no diffuse scattering, unless they strike a wall perpendicularly, in which case the probability of diffusive scattering is the highest<sup>35</sup>. Thus, phonons may ballistically cover a large part of a straight NW, whereas in serpentine NWs their ballistic path would be limited by the length of one segment. Similar blocking of phonon path has been predicted for kinked silicon<sup>38,40</sup> and boron carbide<sup>41</sup> NWs.

Our simulations confirmed that turns of serpentine NWs block the direct flights of some phonons and thus limit their free paths proportionally to the segment length. Due to this limitation of phonon paths, measurements on serpentine NWs seems to yield the thermal conductivity of individual segments. This technique allows us to probe thermal conductivity in NWs shorter than we could probe in our earlier experiments on straight NWs<sup>15,17</sup>.

As we increase the temperature, both wavelengths and mean free path of phonons become shorter making heat conduction more diffusive. Our simulations illustrate how this transition is driven by both more diffusive surface scattering and more frequent internal scattering events. Remarkably, even improving surface roughness cannot delay these temperature-induced changes. Experimentally, we observed that an increase in temperature gradually weakened the ballistic contribution almost independently of the segment length.

Above 150 K, the difference in thermal conductivity of straight and serpentine NWs disappears completely. This result resembles that of a recent experiment by Zhao *et al.*<sup>40</sup>, where

the difference between a straight silicon NW and a NW with one turn quickly dropped as the temperature increased up to 150 K but saturated around 5 – 6 % above this temperature.

Thus, above 150 K we can no longer observe ballistic effects at the length scale of the NW segments ( $> 400$  nm). In some sense, this means that heat conduction becomes diffusive at this scale and temperature. However, in the length-dependent experiments on straight NWs<sup>15</sup>, we could measure deviations from purely diffusive behaviour even up to room temperature. In this sense, heat conduction above 150 K is only quasi-diffusive because it remains quasi-ballistic at the length scales that we cannot probe directly yet can feel *via* non-linear thermal resistance. In this quasi-diffusive regime, the difference in decay time inverses, featuring the corner-cutting effect, recently observed in simulations<sup>15,42</sup>. This geometrical effect naturally depends on the segment length and can be useful for applications requiring both suspension and faster heat dissipation.

Although we could not directly observe quasi-ballistic heat conduction above 150 K, simulations suggest that silicon NWs with better surface quality and lengths shorter than one micron should display quasi-ballistic heat conduction even at room temperature<sup>43,44</sup>. Moreover, simulations<sup>42</sup> predict 10% lower thermal conductivity in serpentine NWs with segments as short as 225 nm. Thus, to experimentally demonstrate ballistic heat conduction in silicon nanostructures at room temperature, future studies should strive for lower surface roughness and shorter length scale of samples.

## Methods

### Samples fabrication

Our samples were fabricated on a silicon-on-insulator wafer with 145-nm-thick device monocrystalline (100) layer and undoped 2- $\mu\text{m}$ -thick  $\text{SiO}_2$  sacrificial layer. First, we deposited 70-nm-thick aluminium squares ( $5 \times 5 \mu\text{m}$ ) using electron beam lithography and electron-beam assisted physical deposition (Ulvac EX-300) processes. Then, top silicon layer was etched using electron beam lithography followed by inductively coupled plasma (ICP) reactive ion etching (RIE)

at  $-145^{\circ}\text{C}$  (Oxford Instruments Plasmalab System 100 ICP) using  $\text{SF}_6$  and  $\text{O}_2$  gases. As a final step, we removed the  $\text{SiO}_2$  sacrificial layer under the samples using hydrofluoric (HF) acid vapour. As a result, silicon island with a metal pad was suspended on four NWs, as shown in Fig. 1a. The surface roughness of our samples was visibly higher than in our previous work<sup>15</sup>. We can estimate the r.m.s. surface roughness to be about 2 nm or higher.

### Errors analysis

One iteration of the  $\mu\text{TDTR}$  experiment consists in integrating the probe laser signal over  $10^4$  pulses of the pump laser. The obtained decay curves are continuously averaged over the last 20 iterations to get the curves shown in Fig. 1d. At each iteration, the algorithm fits the decay curve by  $\exp(-t/\tau)$  function and records  $\tau$  values. This process continues until a standard deviation of  $\tau$  in the last 20 iterations does not become less than 1%, at which point algorithm records the final value of the decay time for the given sample. To account for fabrication imperfection, we fabricated and measured three copies of each sample. The thermal conductivity is extracted for each of the three samples. Thus, each data point in this work shows the average of these three measurements with error bars indicating standard deviation, which typically is 3 – 10%. For plots with the thermal conductivity, the error bars also include an additional 1% uncertainty due to the SEM measurements uncertainty<sup>45</sup>, which affects the FEM simulations.

### Monte Carlo simulations

In our simulations, we use particle approximation of phonons and ray-tracing approach<sup>46</sup> to simulate the phonon transport in a three-dimensional model of our NWs. At the hot side, the algorithm generates 5000 phonons with frequencies according to Planck distribution at the given temperature. The frequency determines the group velocity according to the phonon dispersion ( $\omega(k)$ ) in bulk silicon, with polarization branch chosen randomly (Fig. S4). Generated phonons start moving in a random direction towards the cold side. The algorithm traces phonon trajectories as they travel through NWs and records the lengths of flights between diffusive scattering events, as

well as the projection on the NW axis. Whenever a phonon encounters a boundary, the probability of specular reflection is calculated as  $p = \exp(-16 \pi^2 \eta^2 \cos^2(\alpha) / \lambda^2)$ , where  $\lambda$  is the wavelength,  $\alpha$  is the incidence angle,  $\eta$  is r.m.s. surface roughness<sup>47</sup>. The surface roughness was set to 0.2 nm for the top and bottom surfaces and 2 nm for the sidewall, unless marked otherwise. Moreover, phonons experience internal scattering processes, which cause scattering after time  $t = -\ln(r) \cdot \tau_{\text{int}}$ , where  $r$  is a random number between zero and one, unless a diffuse boundary scattering occurred first<sup>43</sup>. The internal scattering rate is calculated as  $1 / \tau_{\text{int}} = 1 / \tau_{\text{I}} + 1 / \tau_{\text{U}}$ , where  $1 / \tau_{\text{I}} = 2.29 \times 10^{-45} \cdot \omega^4$  is the impurity scattering rate, and  $1 / \tau_{\text{U}} = 0.95 \times 10^{-19} \cdot \omega^2 \cdot T \cdot \exp(-152/T)$  is the Umklapp scattering rate.

## Acknowledgements

This work was supported by Kakenhi (15H05869, 17H02729, and 18K14078), CREST JST (JPMJCR19Q3), and Postdoctoral Fellowship program of Japan Society for the Promotion of Science.

## Conflicts of interest

There are no conflicts to declare.

## References

- 1 E. Pop, *Nano Res.*, 2010, **3**, 147–169.
- 2 M. Nomura, J. Shiomi, T. Shiga and R. Anufriev, *Jpn. J. Appl. Phys.*, 2018, **57**, 080101.
- 3 J. Maire, G. Arregui, N. E. Capuj, M. F. Colombano, A. Griol, A. Martinez, C. M. Sotomayor-Torres and D. Navarro-Urrios, *APL Photonics*, 2018, **3**, 126102.
- 4 J. Gomis-Bresco, D. Navarro-Urrios, M. Oudich, S. El-Jallal, A. Griol, D. Puerto, E. Chavez, Y. Pennec, B. Djafari-Rouhani, F. Alzina, A. Martínez and C. M. S. S. Torres, *Nat. Commun.*, 2014, **5**, 4452.
- 5 I. J. Maasilta, T. A. Puurtinen, Y. Tian and Z. Geng, *J. Low Temp. Phys.*, 2015, **184**, 211–216.
- 6 I. J. Maasilta and T. Kühn, *J. Low Temp. Phys.*, 2008, **151**, 64–69.
- 7 A. N. Bolgar, J. I. Zotova, D. D. Kirichenko, I. S. Besedin, A. V. Semenov, R. S. Shaikhaidarov and O. V. Astafiev, *Phys. Rev. Lett.*, 2018, **120**, 223603.

- 8 A. D. O'Connell, M. Hofheinz, M. Ansmann, R. C. Bialczak, M. Lenander, E. Lucero, M. Neeley, D. Sank, H. Wang, M. Weides, J. Wenner, J. M. Martinis and A. N. Cleland, *Nature*, 2010, **464**, 697–703.
- 9 R. Manenti, A. F. Kockum, A. Patterson, T. Behrle, J. Rahamim, G. Tancredi, F. Nori and P. J. Leek, *Nat. Commun.*, 2017, **8**, 975.
- 10 K. T. Regner, J. P. Freedman and J. a. Malen, *Nanoscale Microscale Thermophys. Eng.*, 2015, **19**, 183–205.
- 11 K. T. Regner, D. P. Sellan, Z. Su, C. H. Amon, A. J. H. H. McGaughey and J. A. Malen, *Nat. Commun.*, 2013, **4**, 1640.
- 12 N. K. Ravichandran, H. Zhang and A. J. Minnich, *Phys. Rev. X*, 2018, **8**, 041004.
- 13 A. A. Maznev, *Phys. Rev. B - Condens. Matter Mater. Phys.*, 2015, **91**, 134306.
- 14 Stefano Lepri, *Thermal Transport in Low Dimensions: From Statistical Physics to Nanoscale*, 2016.
- 15 R. Anufriev, S. Gluchko, S. Volz and M. Nomura, *ACS Nano*, 2018, **12**, 11928–11935.
- 16 N. Yang, G. Zhang and B. Li, *Nano Today*, 2010, **5**, 85–90.
- 17 J. Maire, R. Anufriev and M. Nomura, *Sci. Rep.*, 2017, **7**, 41794.
- 18 F. Zhuge, T. Takahashi, M. Kanai, K. Nagashima, N. Fukata, K. Uchida and T. Yanagida, *J. Appl. Phys.*, 2018, **124**, 065105.
- 19 A. Tavakoli, K. Lulla, T. Crozes, N. Mingo, E. Collin and O. Bourgeois, *Nat. Commun.*, 2018, **9**, 4287.
- 20 T.-K. Hsiao, H.-K. Chang, S.-C. Liou, M.-W. Chu, S.-C. Lee and C.-W. Chang, *Nat. Nanotechnol.*, 2013, **8**, 534–8.
- 21 B.-W. W. Huang, T.-K. K. Hsiao, K.-H. H. Lin, D.-W. W. Chiou and C.-W. W. Chang, *AIP Adv.*, 2015, **5**, 053202.
- 22 T. K. Hsiao, B. W. Huang, H. K. Chang, S. C. Liou, M. W. Chu, S. C. Lee and C. W. Chang, *Phys. Rev. B*, 2015, **91**, 035406.
- 23 Q. Zhang, C. Liu, X. Liu, J. Liu, Z. Cui, Y. Zhang, L. Yang, Y. Zhao, T. T. Xu, Y. Chen, J. Wei, Z. Mao and D. Li, *ACS Nano*, 2018, **12**, 2634–2642.
- 24 V. Lee, C. H. Wu, Z. X. Lou, W. L. Lee and C. W. Chang, *Phys. Rev. Lett.*, 2017, **118**, 135901.
- 25 A. A. Balandin, *Nat. Mater.*, 2011, **10**, 569–581.
- 26 C. W. Chang, D. Okawa, H. Garcia, A. Majumdar and A. Zettl, *Phys. Rev. Lett.*, 2008, **101**, 075903.
- 27 X. Xu, L. F. C. C. Pereira, Y. Wang, J. Wu, K. Zhang, X. Zhao, S. Bae, C. Tinh Bui, R. Xie, J. T. L. L. Thong, B. H. Hong, K. P. Loh, D. Donadio, B. Li and B. Özyilmaz, *Nat. Commun.*, 2014, **5**, 3689.

- 28 M.-H. H. Bae, Z. Li, Z. Aksamija, P. N. Martin, F. Xiong, Z.-Y. Y. Ong, I. Knezevic and E. Pop, *Nat. Commun.*, 2013, **4**, 1734.
- 29 C.-W. Chang, *AAPS Bull.*, 2018, **28**, 15–22.
- 30 Q.-Y. Li, K. Takahashi and X. Zhang, *Phys. Rev. Lett.*, 2017, **119**, 179601.
- 31 J. A. Johnson, A. A. Maznev, J. Cuffe, J. K. Eliason, A. J. Minnich, T. Kehoe, C. M. S. Torres, G. Chen and K. A. Nelson, *Phys. Rev. Lett.*, 2013, **110**, 025901.
- 32 J. B. Hertzberg, M. Aksit, O. O. Otelaja, D. A. Stewart and R. D. Robinson, *Nano Lett.*, 2014, **14**, 403–415.
- 33 S. Natarajan Raja, R. Rhyner, K. Vuttivorakulchai, M. Luisier, D. Poulikakos, S. N. Raja, R. Rhyner, K. Vuttivorakulchai, M. Luisier, D. Poulikakos, S. Natarajan Raja, R. Rhyner, K. Vuttivorakulchai, M. Luisier, D. Poulikakos, S. N. Raja, R. Rhyner, K. Vuttivorakulchai, M. Luisier and D. Poulikakos, *Nano Lett.*, 2016, **17**, 276–283.
- 34 J. S. Heron, C. Bera, T. Fournier, N. Mingo and O. Bourgeois, *Phys. Rev. B*, 2010, **82**, 155458.
- 35 R. Anufriev, A. Ramiere, J. Maire and M. Nomura, *Nat. Commun.*, 2017, **8**, 15505.
- 36 R. Anufriev, R. Yanagisawa and M. Nomura, *Nanoscale*, 2017, **9**, 15083–15088.
- 37 J. Maire, R. Anufriev, T. Hori, J. Shiomi, S. Volz and M. Nomura, *Sci. Rep.*, 2018, **8**, 4452.
- 38 J. W. Jiang, N. Yang, B. S. Wang and T. Rabczuk, *Nano Lett.*, 2013, **13**, 1670–1674.
- 39 P. Jiang, L. Lindsay and Y. K. Koh, *J. Appl. Phys.*, 2015, **119**, 245705.
- 40 Y. Zhao, L. Yang, C. Liu, Q. Zhang, Y. Chen, J. Yang and D. Li, *Int. J. Heat Mass Transf.*, 2019, **137**, 573–578.
- 41 Q. Zhang, Z. Cui, Z. Wei, S. Y. Chang, L. Yang, Y. Zhao, Y. Yang, Z. Guan, Y. Jiang, J. Fowlkes, J. Yang, D. Xu, Y. Chen, T. T. Xu and D. Li, *Nano Lett.*, 2017, **17**, 3550–3555.
- 42 W. Park, G. Romano, E. C. Ahn, T. Kodama, J. Park, M. T. Barako, J. Sohn, S. J. Kim, J. Cho, A. M. Marconnet, M. Asheghi, A. M. Kolpak and K. E. Goodson, *Sci. Rep.*, 2017, **7**, 6233.
- 43 M. Upadhyaya and Z. Aksamija, *Phys. Rev. B*, 2016, **94**, 174303.
- 44 L. Ma, R. Mei, M. Liu, X. Zhao, Q. Wu and H. Sun, *Appl. Therm. Eng.*, 2017, **124**, 17–21.
- 45 R. Anufriev, J. Maire and M. Nomura, *Phys. Rev. B*, 2016, **93**, 045411.
- 46 Y. C. Hua and B. Y. Cao, *Nanoscale Microscale Thermophys. Eng.*, 2017, **21**, 159–176.
- 47 S. B. Soffer, *J. Appl. Phys.*, 1967, **38**, 1710.

